International Journal of Machine Tools & Manufacture 53 (2012) 39–50

Contents lists available at SciVerse ScienceDirect

International Journal of Machine Tools & Manufacture

journal homepage: www.elsevier.com/locate/ijmactool

Modeling and experimentation for three-dimensional dynamics of endmills

Bekir Bediz [a], Uttara Kumar [b], Tony L. Schmitz [c], O. Burak Ozdoganlar [a,*]

[a] Department of Mechanical Engineering, Carnegie Mellon University, Pittsburgh, PA 15213, USA
[b] Department of Mechanical and Aerospace Engineering, University of Florida, Gainesville, FL 32611, USA
[c] Department of Mechanical Engineering and Engineering Science, University of North Carolina at Charlotte, Charlotte, NC 28223, USA

ARTICLE INFO

Article history:
Received 11 May 2011
Received in revised form
12 September 2011
Accepted 13 September 2011
Available online 22 September 2011

Keywords:
Endmill dynamics
Three-dimensional spectral Tchebychev
Modal analysis
Receptance coupling substructure analysis

ABSTRACT

This paper presents a model for the three-dimensional (3D) dynamic response of endmills while considering the actual fluted cross-sectional geometry and pretwisted shape of the tools. The model is solved using the spectral-Tchebychev (ST) technique. The bending and the coupled torsional-axial behavior of four different fluted endmills is compared to finite element model (FEM) predictions and experimental results obtained using modal testing under free-free boundary conditions. For the first eight modes, including six bending and two torsional/axial modes, the difference between the 3D-ST and experimental natural frequencies is shown to be 3% or less for all four tools tested during this study. For the same modes, the 3D-ST and FEM predictions agree to better than 1%. To demonstrate its application, the 3D-ST model for the fluted section of a commercial endmill is coupled to the spindle–holder to predict the tool-point dynamics using receptance coupling substructure analysis (RCSA) with a flexible connection. The coupled model is validated through experiments.

1. Introduction

The dynamic behavior of the tool–holder–spindle–machine assembly, as reflected at cutting points along a milling tool, often determines the achievable process efficiency and quality that can be obtained during milling. The combination of the cutting mechanics, which describe the machining forces for the selected machining conditions, tool geometry, and relative tool-workpiece motion; and the structural dynamics, which dictate the relative tool-workpiece motion at the cutting point in response to the machining forces, determine the dynamic behavior of machining operations [1–3]. The structural dynamics include the dynamic behavior of the entire structural assembly, including the tool, holder, spindle, and machine. Unless cutting conditions and tool geometry are selected carefully, the mechanics–dynamics interaction can cause unstable cutting conditions (chatter) due to the over-cutting of the surface left by one tooth of the vibrating cutter by subsequent teeth. Even under stable cutting conditions, forced vibrations of the flexible tool can lead to errors in the location of the machined surface (in milling). If the dynamic response is well-known, however, models can be applied to guide selection of cutting conditions that increase stability and reduce surface location errors.

In order to accurately predict the tool–holder–spindle–machine (THSM) assembly dynamics, two fundamental capabilities are needed: (1) accurate and numerically efficient dynamic models of realistic, arbitrary tool and holder geometries that capture non-symmetric bending and coupled torsional/axial dynamics; and (2) a means to join the experimentally determined spindle–machine dynamics to the model-based tool–holder dynamics to obtain the THSM assembly dynamics at any point along the tool [4–13].

This paper describes new results for modeling three-dimensional dynamic behavior of macro-scale milling tools using the spectral-Tchebychev[1] (ST) technique while considering the actual fluted geometry. The 3D-ST model results for both bending and torsion are compared to finite element computations and experimental data obtained using impact testing with free–free boundary conditions. The 3D-ST model for the actual geometry of the fluted portion of the tool is then combined with the holder model and the measured spindle dynamics to predict the THSM assembly dynamics through receptance coupling substructure analysis (RCSA).

2. Modeling and spectral-Tchebychev solution of macro-endmill dynamics

This section briefly describes the derivation of the endmill dynamics model and the associated 3D-ST technique used to solve the model numerically. The approach outlined here follows

* Corresponding author. Tel.: +1 412 268 9890; fax: +1 412 268 3348.
E-mail address: ozdoganlar@cmu.edu (O. Burak Ozdoganlar).

[1] The name of the Russian mathematician P.L. Tchebychev can be alternatively transliterated as Chebychev or Chebyschev.

0890-6955/$ - see front matter © 2011 Elsevier Ltd. All rights reserved.
doi:10.1016/j.ijmachtools.2011.09.005

that presented (and experimentally validated) by Filiz and Ozdoganlar [14,15].

A traditional macro-scale endmill can be represented by the diameter of the shank section (commonly referred to as the tool diameter, d_s), helix angle Ψ, the shank length L_s, the flute length L_f, number of flutes, and the cross-sectional geometry of the fluted region. Due to its simple circular cross-section, the axial, torsional, and bending deflections of the shank region are uncoupled. Thus, an appropriate one-dimensional (1D) beam models (e.g., the Timoshenko beam model) is sufficient to describe the dynamics of the shank. However, the fluted section with its pre-twisted geometry and complex cross-section causes the axial and torsional deflections to be coupled. Furthermore, unlike those of the shank portion, bending deflections of the fluted portion are not symmetric. As a result, accurately capturing the dynamic behavior of the fluted section necessitates use of 3D modeling techniques. Therefore, to simultaneously achieve numerical efficiency and modeling accuracy, a 1D model for the shank and a 3D model for the fluted section are used. The extended Hamilton's principle is applied to obtain the integral boundary value problem for the each of the shank and fluted sections. The complete model is then obtained by combining the shank (1D) and fluted (3D) portions through component mode synthesis.

2.1. Solution of the 1D-ST for the dynamics of the shank

To insure the accuracy of the dynamic model, particularly for higher modes, the Timoshenko beam model, which includes the shear and rotary inertia effects, is used to model the 1D dynamics of the shank section [16,17]. The model includes bending, axial, and torsional motions of the shank section. Following the extended Hamilton's principle, the integral boundary value problem for the 1D model can be expressed as

$$\begin{aligned}\int_0^L \Bigg[& \rho A\frac{\partial^2 u}{\partial t^2}\hat{u}+\rho I_x\frac{\partial^2 \psi_y}{\partial t^2}\hat{\psi}_y+\rho A\frac{\partial^2 v}{\partial t^2}\hat{v}+\rho I_y\frac{\partial^2 \psi_x}{\partial t^2}\hat{\psi}_x \\ & +\rho A\frac{\partial^2 w}{\partial t^2}\hat{w}+\rho I_p\frac{\partial^2 \psi_z}{\partial t^2}\hat{\psi}_z \\ & +EI_x\frac{\partial \psi_y}{\partial z}\frac{\partial \hat{\psi}_y}{\partial z}+k_sGA\left(\frac{\partial u}{\partial z}-\psi_y\right)\left(\frac{\partial \hat{u}}{\partial z}-\hat{\psi}_y\right)+EI_y\frac{\partial \psi_x}{\partial z}\frac{\partial \hat{\psi}_x}{\partial z} \\ & +k_sGA\left(\frac{\partial v}{\partial z}+\psi_x\right)\left(\frac{\partial \hat{v}}{\partial z}+\hat{\psi}_x\right)+EA\frac{\partial w}{\partial z}\frac{\partial \hat{w}}{\partial z} \\ & +GJ_s\frac{\partial \psi_z}{\partial z}\frac{\partial \hat{\psi}_z}{\partial z}\Bigg]dz=\int_0^L \{F_q\}^T\{\hat{q}\}\,dz, \end{aligned} \tag{1}$$

where $\{\hat{q}\}^T=\{\hat{u}\ \hat{v}\ \hat{w}\ \hat{\phi}_x\ \hat{\phi}_y\ \hat{\phi}_z\}^T$ are the functions representing the variation terms, L is the length of the beam, ρ is the density, $A(z)$ is the cross-sectional area along the beam axis, E is Young's modulus, G is the shear modulus, $I_p(z)$ is the polar moment of inertia, $J_s(z)$ is the torsion constant, $I_x(z)$ and $I_y(z)$ are the second area moments, k_s is the shear constant, and x and y are the angular deflections of the beam due to shear deformations.

The solution of Eq. (1) is obtained using the 1D spectral-Tchebychev technique described by Yagci et al. [18]. The generalized coordinates are sampled in the spatial domain, and expressed as a truncated series expansion of orthogonal Tchebychev polynomials as

$$q_i \cong \sum_{n_z=1}^{N_z} a_{qi}(t)T_{n_z-1}(z), \tag{2}$$

where q_i is the generalized coordinate, T_{n_z-1} are the scaled Tchebychev polynomials, N_z is the number of polynomials used in expanding the generalized coordinate, and a_{qi} are the time-dependent expansion coefficients. The derivative and inner product operations are defined in the sampled domain and can be given as

$$\underline{q}_i^n=Q_n\underline{q}_i \quad \text{and} \quad \int_0^L A(z)q(z)\hat{q}(z)\,dz=\underline{q}^T V_A\underline{\hat{q}}, \tag{3}$$

where Q_n is the nth derivative matrix, V_A is the inner product matrix and the underline indicates the sampled functions based on Gauss–Lobatto sampling. The deflections associated with each of the six degrees-of-freedom for each of the sample points can be described in terms of q, e.g.

$$\underline{u}=[\mathbb{I}\ \mathbb{O}\ \mathbb{O}\ \mathbb{O}\ \mathbb{O}\ \mathbb{O}]\underline{q}=\mathbb{I}_u\underline{q}, \tag{4}$$

$$\underline{\psi_x}=[\mathbb{O}\ \mathbb{O}\ \mathbb{O}\ \mathbb{I}\ \mathbb{O}\ \mathbb{O}]\underline{q}=\mathbb{I}_{\psi_x}\underline{q}. \tag{5}$$

Substituting Eqs. (2)–(4) in Eq. (1) and using the weighted residual method, the mass, stiffness and forcing matrices can be obtained as

$$\begin{aligned}M=P^T\rho(&\mathbb{I}_u^TV_A\mathbb{I}_u+\mathbb{I}_{\psi_y}^TV_{I_x}\mathbb{I}_{\psi_y}+\mathbb{I}_v^TV_A\mathbb{I}_v+\mathbb{I}_{\psi_x}^TV_{I_y}\mathbb{I}_{\psi_x}V_A \\ &+\mathbb{I}_w^T\mathbb{I}_w+\mathbb{I}_{\psi_z}^TV_{I_p}\mathbb{I}_{\psi_z})P,\end{aligned} \tag{6}$$

$$\begin{aligned}K=P^T[&E\mathbb{Q}_{\psi_y}^TV_{I_x}\mathbb{Q}_{\psi_y}+k_sG(\mathbb{Q}_u-\mathbb{I}_{\psi_y})^TV_A(\mathbb{Q}_u-\mathbb{I}_{\psi_y})+E\mathbb{Q}_{\psi_x}^TV_{I_y}\mathbb{Q}_{\psi_x} \\ &+k_sG(\mathbb{Q}_v+\mathbb{I}_{\psi_x})^TV_A(\mathbb{Q}_v+\mathbb{I}_{\psi_x})+E\mathbb{Q}_w^TV_A\mathbb{Q}_w+G\mathbb{Q}_{\psi_z}^TV_{J_s}\mathbb{Q}_{\psi_z}]P,\end{aligned} \tag{7}$$

$$\begin{aligned}F=P^TV\underline{F}_q-P^T\rho(&\mathbb{I}_u^TV_A\mathbb{I}_u+\mathbb{I}_{\psi_y}^TV_{I_x}\mathbb{I}_{\psi_y}+\mathbb{I}_v^TV_A\mathbb{I}_v+\mathbb{I}_{\psi_x}^TV_{I_y}\mathbb{I}_{\psi_x} \\ &+\mathbb{I}_w^TV_A\mathbb{I}_w+\mathbb{I}_{\psi_z}^TV_{I_p}\mathbb{I}_{\psi_z})R\ddot{q}_b-P^T[E\mathbb{Q}_{\psi_y}^TV_{I_x}\mathbb{Q}_{\psi_y} \\ &+k_sG(\mathbb{Q}_u-\mathbb{I}_{\psi_y})^TV_A(\mathbb{Q}_u-\mathbb{I}_{\psi_y})+E\mathbb{Q}_{\psi_x}^TV_{I_y}\mathbb{Q}_{\psi_x} \\ &+k_sG(\mathbb{Q}_v+\mathbb{I}_{\psi_x})^TV_A(\mathbb{Q}_v+\mathbb{I}_{\psi_x})+E\mathbb{Q}_w^TV_A\mathbb{Q}_w+G\mathbb{Q}_{\psi_z}^TV_{J_s}\mathbb{Q}_{\psi_z}]Rq_b.\end{aligned} \tag{8}$$

2.2. Solution of the 3D-ST for the dynamics of the fluted section

The fluted section and the transition region (from the flutes to the shank sections) are modeled using 3D dynamics. For a 3D structure, axial, torsional, and bending motions are coupled. To obtain the boundary-value problem (BVP) for the 3D deflections of the fluted section, 3D linear elasticity theory is used to obtain the strain (elastic) energy. Using the extended Hamilton's principle and applying integration by parts, the integral BVP for the fluted section can be obtained as

$$\int_{t_1}^{t_2}\int_{Volume}[\rho\,\{\ddot{q}\}^T\{\hat{q}\}-\{q\}^T[B]^T[B_C]\{\hat{q}\}+\{F_q\}^T\{\hat{q}\}]\,dx\,dy\,dz\,dt=0, \tag{9}$$

where $\{F_q\}=\{F_x\ F_y\ F_z\}^T$. In arriving at the BVP given in Eq. (9), the stress–strain (constitutive) equations were $\{\sigma\}=\{C\}\{\varepsilon\}$, where C is the constitutive matrix, and the strain-displacement relations were $\{\varepsilon\}=\{B\}\{q\}$, where B is the differential operator matrix.

In order to solve the 3D fluted section problem defined by Eq. (9) using the 3D-ST method, coordinate transformations and a mapping of the complex cross-sectional flute geometry into a rectangular domain are required. The pretwist effect can be accommodated by using a local coordinate frame $(\overline{x},\overline{y},\overline{z})$, and the complex cross-section defined by the $(\overline{x},\overline{y},\overline{z})$ domain is mapped onto a rectangular cross-section domain defined by the coordinates (ξ,η,ζ). Combining both operations, the relation between the final coordinates (ξ,η,ζ) and the physical domain (x,y,z) can be written as

$$\frac{\partial}{\partial \overline{x}_i}=J_{ij}^{\overline{x}\,x}\frac{\partial}{\partial x_j} \quad \text{and} \quad \frac{\partial}{\partial \xi_i}=J_{ij}^{\xi\,\overline{x}}\frac{\partial}{\partial \overline{x}_i}, \quad i,j=1,2,3,\ldots, \tag{10}$$

where $J_{ij}^{\overline{x}x}$ and $J_{ij}^{\xi\overline{x}}$ are the elements of the Jacobian matrices of the cross-section transformation and mapping, respectively.

The integral BVP given in Eq. (9) is then solved using the 3D-ST technique. First, each deflection term is expressed using a three-

dimensional Tchebychev (truncated) series expansion

$$q_i(\xi,\eta,\zeta,t) \cong \sum_{l=1}^{N_\xi}\sum_{m=1}^{N_\eta}\sum_{n=1}^{N_\zeta} a_{qi}(t)T_{l-1}(\xi)T_{m-1}(\eta)T_{n-1}(\zeta), \tag{11}$$

where the T terms represent the orthogonal (scaled) Tchebychev polynomials, a_{q_i} are the polynomial coefficients, and N_j is the number of polynomials associated with the coordinate $j=(\xi, \eta, \zeta)$. Similar to the 1D approach, the derivative and inner product operations are defined in the sampled domain as

$$\underline{q}^n_{i,x_i} = Q^{x_i}_n \mathbb{I}_i \underline{q} \quad \text{and} \quad \int_0^L \int_{Area} q\,\hat{q}\,dx\,dy\,dz = \underline{q}^T\,V^{xyz}\,\underline{\hat{q}}, \tag{12}$$

where $\underline{q}^n_{i,x_i}$ is the nth spatial derivative and $Q^{x_i}_n$ is the nth extended derivative matrix with respect to coordinate x_i, and V^{xyz} is the inner product matrix. Similarly as in the 1D solution, the mass, stiffness, and force matrices can be found from Eq. (9) as

$$M = \rho(\mathbb{I}_u^T V^{xyz}\mathbb{I}_u + \mathbb{I}_v^T V^{xyz}\mathbb{I}_v + \mathbb{I}_w^T V^{xyz}\mathbb{I}_w), \tag{13}$$

$$K = \underline{B}^T \mathbb{V}^{xyz}\underline{B}_C, \tag{14}$$

$$F = V^{xyz}\underline{F}_q. \tag{15}$$

2.3. Combining 1D and 3D solutions

The 1D formulation for the shank section provides six deflection components (three displacements and three angles) for a given axial position. The 3D formulation for the fluted section, on the other hand, provides three deflection components for each sampling point at given three-dimensional position within the solid. To combine the 1D-ST solution for the shank with the 3D-ST solution for the fluted (and transition) regions, and thus, to form a global boundary value problem, compatibility conditions are used at the boundaries shared by the two sections. The compatibility equations relate the three displacement degrees of freedom (u, v, w) from the 3D model and the six degrees of freedom ($\overline{u}$, $\overline{v}$, $\overline{w}$, ψ_x, ψ_y, ψ_z) for the 1D model for each point (x,y) within the (boundary) cross-section. Assuming small angles, this compatibility condition can be expressed mathematically as

$$\{u, v, w\} = \{\overline{u} - y\psi_z, \quad \overline{v} + x\psi_z, \quad \overline{w} + x\psi_y + y\psi_x\}. \tag{16}$$

3. Receptance coupling substructure analysis

To demonstrate the application of the 3D-ST model for obtaining the tool-point dynamics, the RCSA technique is used. Fig. 1 shows the schematic of the THSM assembly used for experimental validation. The free–free response of the fluted portion of the tool was obtained analytically by the 3D-ST technique. Using the three-component RCSA technique for tool point dynamics prediction [7], the modeled holder was coupled to

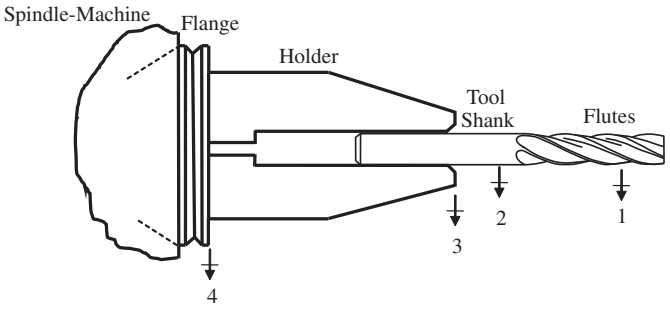

Fig. 1. THSM assembly and coordinates.

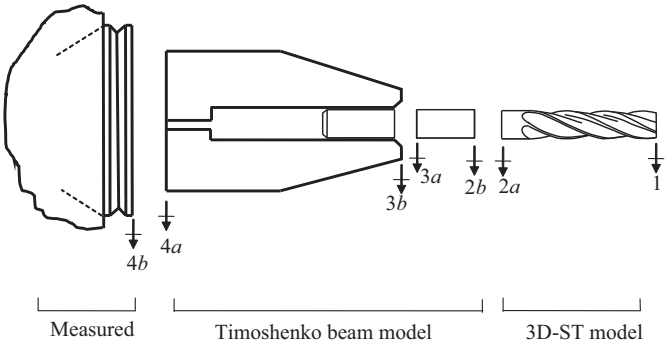

Fig. 2. RCSA components with coordinates.

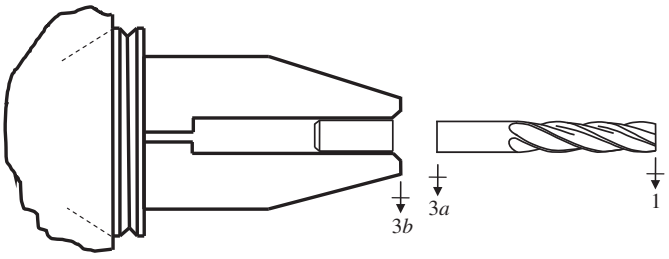

Fig. 3. Component coordinates for flexible coupling.

the archived spindle–machine dynamics and this result was subsequently coupled (using a flexible connection) to the free–free response of the tool. The component coordinates are identified in Figs. 2 and 3.

The receptance matrices for the assembly, G_{ij}, and substructures, R_{ij}, can be represented as shown in Eq. (17), where ω is the frequency, X_i and x_i are the assembly and substructure displacements at the coordinate location i, Θ_i and θ_i are the assembly and substructure rotations, F_j and f_j are the assembly and substructure forces applied at the coordinate location j, and M_j and m_j are the assembly and substructure and moments:

$$G_{ij}(\omega) = \begin{bmatrix} H_{ij} & L_{ij} \\ N_{ij} & P_{ij} \end{bmatrix} = \begin{bmatrix} \frac{X_i}{F_j} & \frac{X_i}{M_j} \\ \frac{\Theta_i}{F_j} & \frac{\Theta_i}{M_j} \end{bmatrix} \quad \text{and} \quad R_{ij}(\omega) = \begin{bmatrix} h_{ij} & l_{ij} \\ n_{ij} & p_{ij} \end{bmatrix} = \begin{bmatrix} \frac{x_i}{f_j} & \frac{x_i}{m_j} \\ \frac{\theta_i}{f_j} & \frac{\theta_i}{m_j} \end{bmatrix}. \tag{17}$$

Using RCSA, the assembly dynamics at coordinate 1 is obtained in two steps. First, the modeled free–free receptances of the holder-shank component are coupled to the free–free receptances of the remainder of the tool (fluted part) using the following:

$$G_{11}\omega = R_{11}\omega - R_{12a}(\omega)[R_{2b2b}(\omega) + R_{2a2a}(\omega)]^{-1}R_{2a1}(\omega), \tag{18}$$

$$G_{3a1}(\omega) = R_{3a2b}(\omega)[R_{2b2b}(\omega) + R_{2a2a}(\omega)]^{-1}R_{2a1}(\omega), \tag{19}$$

$$G_{3a3a}(\omega) = R_{3a3a}(\omega) - R_{3a2b}(\omega)[R_{2b2b}(\omega) + R_{2a2a}(\omega)]^{-1}R_{2b3a}(\omega), \tag{20}$$

$$G_{13a}(\omega) = R_{12a}(\omega)[R_{2b2b}(\omega) + R_{2a2a}(\omega)]^{-1}R_{2b3a}(\omega). \tag{21}$$

This coupling result represents the tool model with end coordinates 1 and 3a (G_{11},G_{13a},G_{3a3a},G_{3a1}). Second, the modeled free–free receptances of the holder with portion of the shank inside it is coupled to the spindle machine receptances:

$$G_{3b3b}(\omega) = R_{3b3b}(\omega) - R_{3b4a}(\omega)[R_{4b4b}(\omega) + R_{4a4a}(\omega)]^{-1}R_{4a3b}(\omega). \tag{22}$$

The free–free receptances are then considered as a component, using the receptance matrices R_{11}, R_{13a}, R_{3a3a} and R_{3a1}. G_{3b3b} is considered as R_{3b3b}. Third, the holder–spindle–machine component is then flexibly coupled to the tool using translational and rotational spring constants assembled in the stiffness matrix k.

The RCSA equation for the flexible coupling tool point FRF [9] is provided as

$$G_{11}(\omega) = R_{11}(\omega) - R_{13a}(\omega)\left[R_{3b3b}(\omega) + R_{3a3a}(\omega) + \frac{1}{k}\right]^{-1} R_{3a1}(\omega). \quad (23)$$

Identification of the stiffness matrix k is discussed in Section 7.

4. Experimental methods

This section describes the experimental setup and procedures used for validating the presented 3D-ST solution. For this purpose, a set of modal tests were conducted on the four different endmills described in Table 1. These four-flute endmills each had different geometries (shank diameter, shank length, flute length, and helix angle). Endmills 1–3 were machined from aluminum blanks so that the cross-sectional geometry was explicitly known; the geometry for the commercial endmill (identified as endmill 4) was determined by sectioning and measurement.

4.1. Description of endmill geometries

The accuracy, and thus effective application, of the 3D-ST solution for macro-endmills requires accurate knowledge of the geometry and material parameters of the endmills. In particular, cross-sectional geometry, twist rate, and the geometry of the transition region (from the shank to the fluted portion) must be well known. To facilitate evaluation of the 3D-ST model for well-known geometries and for a range of geometric parameters, a set of aluminum endmills (test endmills) were fabricated using five-axis machining. Since the aluminum endmills were described using a 3D solid model (SolidWorks®), their geometry was accurately defined within the accuracy of the manufacturing technique. The cross-sectional geometry of the endmills are given in Fig. 4(a).

To enable further assessment of the 3D-ST solution, a commercial (solid) carbide endmill (endmill 4) was selected for testing. However, the detailed information about the cross-sectional geometry was not available. Therefore, the endmill was sectioned by electrical discharge machining (EDM), and the cross-section was imaged at several locations, as shown in Fig. 4(b). The Matlab® image-processing toolbox was then used to identify the boundaries (periphery), and sample points along the periphery were extracted to define the cross-section.

Table 1
Properties of the endmills used for validation experiments (all parameters except the helix angle were measured using digital calipers with a resolution of 0.01 mm).

Properties	Endmill 1	Endmill 2	Endmill 3	Endmill 4
Shank diameter (mm)	38.20	38.17	38.20	12.66
Shank length (mm)	101.35	102.98	77.66	66.40
Flute length (mm)	201.14	175.23	200.44	84.41
Helix angle (mm)	30	30	30	30
Material	Aluminum	Aluminum	Aluminum	Carbide

4.2. Experimental setups and conditions

To determine the natural frequencies of the aluminum endmills, the frequency response functions (FRFs) of the endmills were obtained by impact testing. Fig. 5 shows the experimental procedure used to obtain the bending and torsional natural frequencies of the endmill. To approximate the unconstrained boundary conditions, the endmills were placed on soft foam. The very low stiffness of the foam base relative to the endmills provided a reasonable approximation to unconstrained (free–free) boundary conditions. The FRFs were measured by exciting them using a miniature impact hammer (PCB 0841A17, sensitivity 46.95 N/V) and recording the corresponding vibration using a low mass accelerometer (PCB 352C23, sensitivity 1727 (m/V s^2)). To assess the effect of the miniature accelerometer in the measured dynamic response, a set of finite elements simulations were conducted. It was seen that the added mass due to accelerometer does not change the natural frequencies by more than 0.05% for the first eight natural frequencies of the tool. Therefore, the effect of the miniature accelerometer is deemed negligible.

Depending on the locations of the accelerometer and hammer impact, direct and cross FRFs, H_{ij}, were obtained, where i and j represents the measurement and force locations, respectively. For instance, in the configuration shown in Fig. 5(a), the accelerometer was placed at the shank end, and the force was applied at the same location (from the other side of the endmill). Therefore, the direct FRF at the endmill's shank end was obtained.

Fig. 5(b) shows the experimental procedure used to identify the torsional natural frequencies. The endmill was excited by applying the force to one flute in the tangential direction and the response was recorded in the same direction using an accelerometer placed on the opposite flute. In these experiments both the bending and the torsional natural frequencies were excited. The results for the first eight natural frequencies were recorded.

The resonant frequencies of the solid carbide endmill span a considerably wider range than those of the aluminum endmills. Therefore, the hammer impact test described above cannot be effectively used to determine the first eight natural frequencies of endmill 4.

Fig. 6(a) shows the experimental setup used for obtaining the natural frequencies of the solid carbide endmills. The endmill was suspended using flexible elastic bands from two sections along its length to approximate unconstrained boundary conditions. The dynamic excitations within a frequency range of 0–40 kHz were provided using a 3 mm by 4 mm piezoelectric element with a

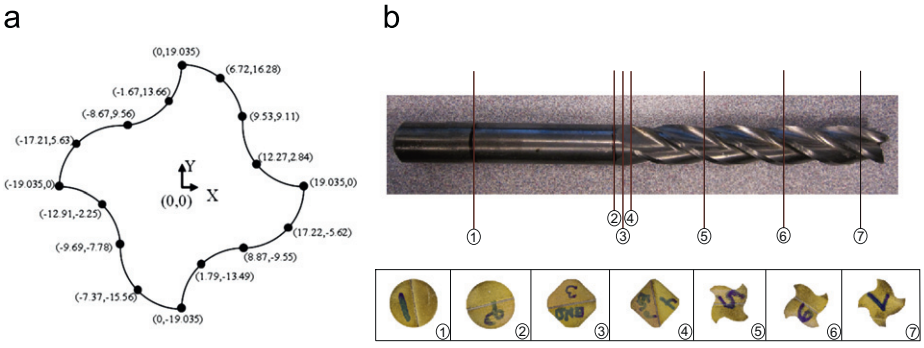

Fig. 4. Cross-section of (a) endmills 1–3 (coordinates are provided in mm), (b) endmill 4.

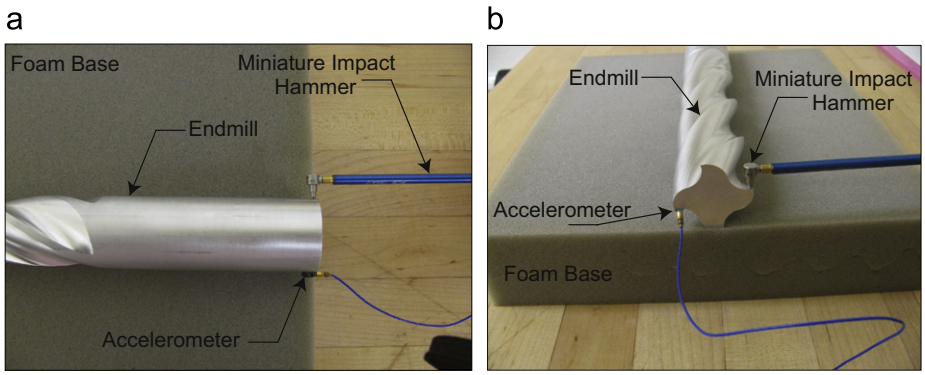

Fig. 5. Impact hammer experimentation setup (a) direct FRF measurement at the endmill shank end and (b) torsional measurement.

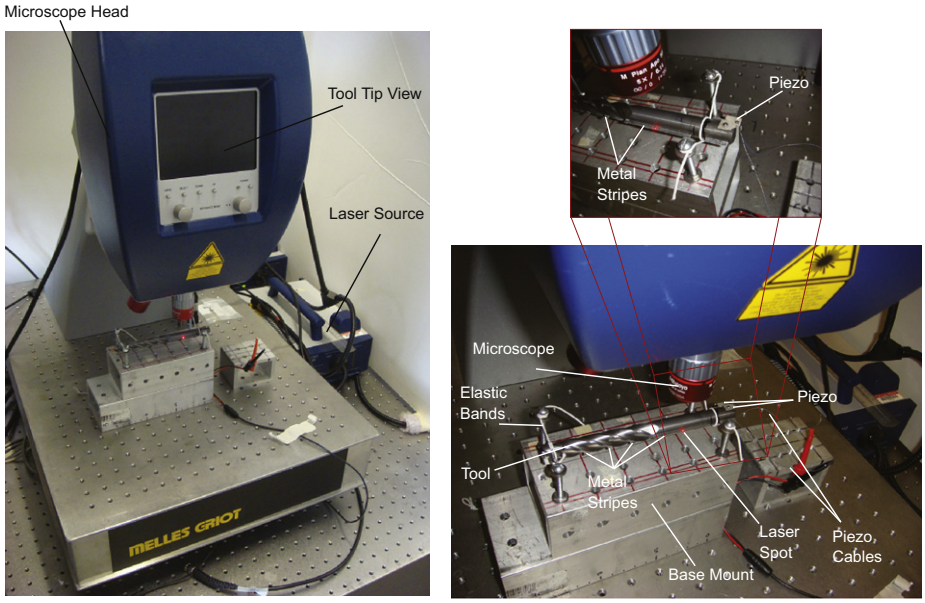

Fig. 6. Experimental setup for endmill 4 free–free boundary condition measurements.

125 μm thickness. As shown in Fig. 6(b), the piezoelectric element was glued onto the macro endmill shank. When a voltage is applied, the piezoelectric element expands and contracts along its polarization axis. A pseudo-random excitation having a range of 0–40 kHz with 140 V amplitude was supplied to the piezoelectric element. For each experiment, 50 measurements of 0.320 s each were completed and averaged to eliminate unbiased noise.

The response is measured using a laser Doppler vibrometer (LDV) system (Polytec® MSA-400) with two fiber-optic laser sources. Each fiber-optic laser source splits into a pair of channels and, therefore, both relative and absolute measurements can be performed. During the experiments, the fiber-optic laser sources were fed through a microscope to reduce the laser-beam spot sizes. For the measurements presented in this study, a $5\times$ objective is used to obtain a spot size of 2.8 μm was used.

The axis of the endmill is located in the vicinity of the nodal line of the torsional motions. Therefore, measurements along the axis of the endmill do not provide accurate determination of the torsional modes. To facilitate measuring the torsional modes, metal strips (0.22 mm by 3.12 mm) were glued to the sides of the macro endmill. The response measured from the metal strips amplifies the torsional motions, thereby enabling accurate determination of torsional/axial natural frequencies.

5. Alternative modeling techniques for comparative analysis

In this section, two alternative approaches for modeling the dynamics of Table 1 endmills are described. The main purpose of this study is to provide a comparative analysis of the 3D-ST technique with two other popular solution approaches. First, a finite element (FE) solution of the endmill dynamics using a commercial solver is outlined. Next, simplified 1D solution of the endmill dynamics using four different equivalent cross-section formulations is provided.

5.1. Finite element modeling (FEM) of macro-endmills

Using the geometry of the four endmills, finite element (FE) models were constructed. Analysis was performed on the meshed solid model of each endmill using the commercial software ANSYS® Workbench (SOLID186 elements). Table 2 lists the material properties (Young's modulus E, density, ρ, and Poisson's ratio, ν). Modal analysis was used to identify the natural frequencies.

The convergence of the FE model was evaluated for all endmills based on the changes in the second torsional natural frequency to ensure that a sufficient number of elements were included. Table 3 summarizes the convergence study for the FE model of endmill 1. The convergence study was performed in a consecutive way, where the percent change in natural frequencies

Table 2
Endmill material properties.

Endmill material	E (GPa)	$\rho\left(\frac{kg}{m^3}\right)$	v
Aluminum	70	2700	0.33
Carbide	580	14 500	0.24

Table 3
Convergence study for endmill 1 from Table 1.

Second torsional natural frequency (Hz)	Number of nodes	Number of elements	% Change in natural frequencies with increasing number of nodes
7776.5	3056	578	–
7756.3	4077	792	−0.26
7746.3	7226	1485	−0.13
7742.4	20 689	4488	−0.05
7739.3	22 454	4828	−0.04

Table 4
Equivalent diameter of endmills.

Endmill	d_{eq_A} (mm)	d_{eq_I} (mm)	d_{eq_V} (mm)	d_{eq_M} (mm)
Aluminum	30.40	31.10	30.96	31.55
Carbide	9.90	10.10	9.95	9.92

were calculated between the two consecutive FE simulations taking the finer meshed model as reference.

5.2. Equivalent diameter approach

One of the common approaches to describe the dynamics of the fluted section is to approximate it as a uniform circular cross-section beam with an equivalent diameter. Four methods were applied to calculate this diameter: (1) the cross-sectional area; (2) the area moment of inertia of the cross-section; (3) the volume; and (4) the mass.

1. The cross-sectional area of the fluted portion, A_f, was obtained from the solid model (endmills 1–3) or analysis of cross-section image (endmill 4) and the corresponding equivalent diameter, d_{eq_A}, was calculated using

$$d_{eq_A} = \sqrt{\frac{4\,A_f}{\pi}}. \tag{24}$$

2. The area moment of inertia for the modeled cross-section of the fluted portion, I_f, was determined and the equivalent diameter, d_{eq_I}, was calculated using

$$d_{eq_I} = \left(\frac{64\,I_f}{\pi}\right)^{1/4}. \tag{25}$$

3. The volume of the fluted section, V_f, was obtained and the equivalent diameter was determined as

$$d_{eq_V} = \sqrt{\frac{4\,V_f}{\pi\,L_f}}. \tag{26}$$

Table 5
Comparison of the experimental and predicted natural frequencies.

Endmill 1	B_{11}	B_{12}	B_{21}	B_{22}	TA_1	B_{31}	B_{32}	TA_2
Experiment (Hz)	1426	1430	4059	4068	4218	7530	7543	7777
FE (Hz)	1400	1403	4000	4002	4115	7484	7492	7739
3D-ST (Hz)	1404	1407	4007	4023	4091	7486	7497	7750
Difference (%) between ST and FEM	0.28	0.32	0.17	0.53	−0.60	0.03	0.06	0.14
Difference (%) between FE and experiment	−1.81	−1.92	−1.45	−1.62	−2.42	−0.61	−0.68	−0.49
Difference (%) between ST and experiment	−1.54	−1.60	−1.28	−1.10	−3.00	−0.58	−0.62	−0.34
Endmill 2	B_{11}	B_{12}	TA_1	B_{21}	B_{22}	TA_2	B_{31}	B_{32}
Experiment (Hz)	1710	1717	4716	4802	4811	8558	8698	8719
FE (Hz)	1691	1691	4606	4776	4776	8523	8673	8674
3D-ST (Hz)	1690	1695	4583	4772	4790	8563	8665	8680
Difference (%) between ST and FEM	−0.06	0.22	−0.51	−0.08	0.30	0.47	−0.09	0.07
Difference (%) between FE and experiment	−1.12	−1.47	−2.32	−0.55	−0.72	−0.40	−0.28	−0.52
Difference (%) between ST and experiment	−1.18	−1.26	−2.81	−0.63	−0.43	0.06	−0.37	−0.45
Endmill 3	B_{11}	B_{12}	TA_1	B_{21}	B_{22}	TA_2	B_{31}	B_{32}
Experiment (Hz)	1634	1638	4414	4588	4596	8412	8602	8615
FE (Hz)	1611	1611	4349	4523	4524	8286	8556	8558
3D-ST (Hz)	1612	1615	4315	4529	4551	8293	8561	8568
Difference (%) between ST and FEM	0.07	0.21	−0.79	0.13	0.60	0.09	0.06	0.13
Difference (%) between FE and experiment	−1.40	−1.64	−1.46	−1.42	−1.57	−1.49	−0.54	−0.66
Difference (%) between ST and experiment	−1.34	−1.43	−2.24	−1.30	−0.98	−1.41	−0.48	−0.54
Endmill 4	B_{11}	B_{12}	B_{21}	B_{22}	TA_1	B_{31}	B_{32}	TA_2
Experiment (Hz)	2487	2487	7343	7343	11273	13515	13515	20071
FE (Hz)	2463	2471	7242	7248	11365	13283	13336	20143
3D-ST (Hz)	2486	2495	7271	7272	11384	13337	13393	20163
Difference (%) between ST and FEM	0.93	0.98	0.40	0.33	0.17	0.41	0.43	0.10
Difference (%) between FE and experiment	−0.96	−0.64	−1.37	−1.29	0.82	−1.72	−1.33	−0.36
Difference (%) between ST and experiment	−0.05	0.33	−0.98	−0.96	0.99	−1.32	−0.91	0.46

4. The mass of the endmill, m, can be expressed as the sum of the mass of the shank (first expression on the left hand side of Eq. (27)) and the mass of the fluted portion (second expression)

$$\rho \frac{\pi d_s^2 L_s}{4} + \rho \frac{\pi d_{eq_M}^2 L_f}{4} = m, \tag{27}$$

where d_{eqM} is the equivalent diameter of the fluted portion. By weighing the endmill and substituting nominal value for the density and geometry of the endmill, the equivalent diameter was calculated according to Eq. (28). The benefit of this approach is that no tool model is required, unlike the first three methods:

$$d_{eq_M} = \sqrt{\frac{4}{\pi L_f}\left(\frac{m}{\rho} - \frac{\pi d_s^2 L_s}{4}\right)}. \tag{28}$$

Table 4 lists the equivalent diameter (inmm) calculated by the four methods for the four endmills.

6. Modal assessment

6.1. Comparison of tool modeling techniques

In this section, the natural frequencies obtained using modal testing, the ST method, and FE model (FEM) simulations are compared to assess the accuracy of the 3D-ST technique for modeling endmill dynamics. Table 5 provides the natural frequencies from 3D-ST, FEM, and experimentation, as well as the percent differences between the modes obtained from different methods. The labeled mode shapes (as bending or torsional/axial) are identified according to the calculated deformations. The bending modes are represented by B_{ij} where i is the mode number and j is the principal direction of deformation. The coupled torsional–axial modes are represented by TA_i where i is the mode number.

For each of the endmills, the percent errors between the ST method and experimentation are seen to be less than 3.0%. This

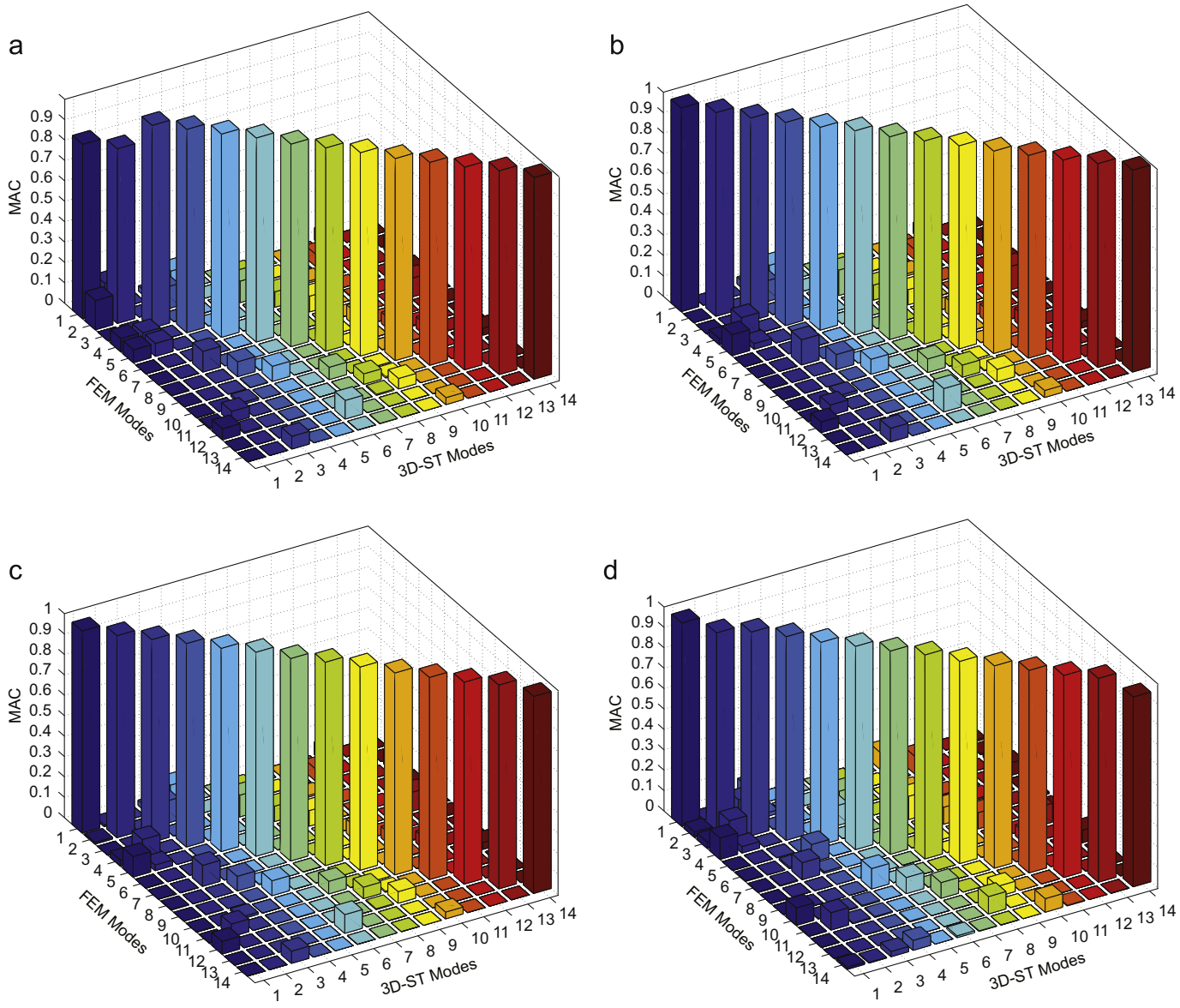

Fig. 7. Modal Assurance Criteria (MAC) analysis for (a) endmill 1; (b) endmill 2; (c) endmill 3; and (d) endmill 4.

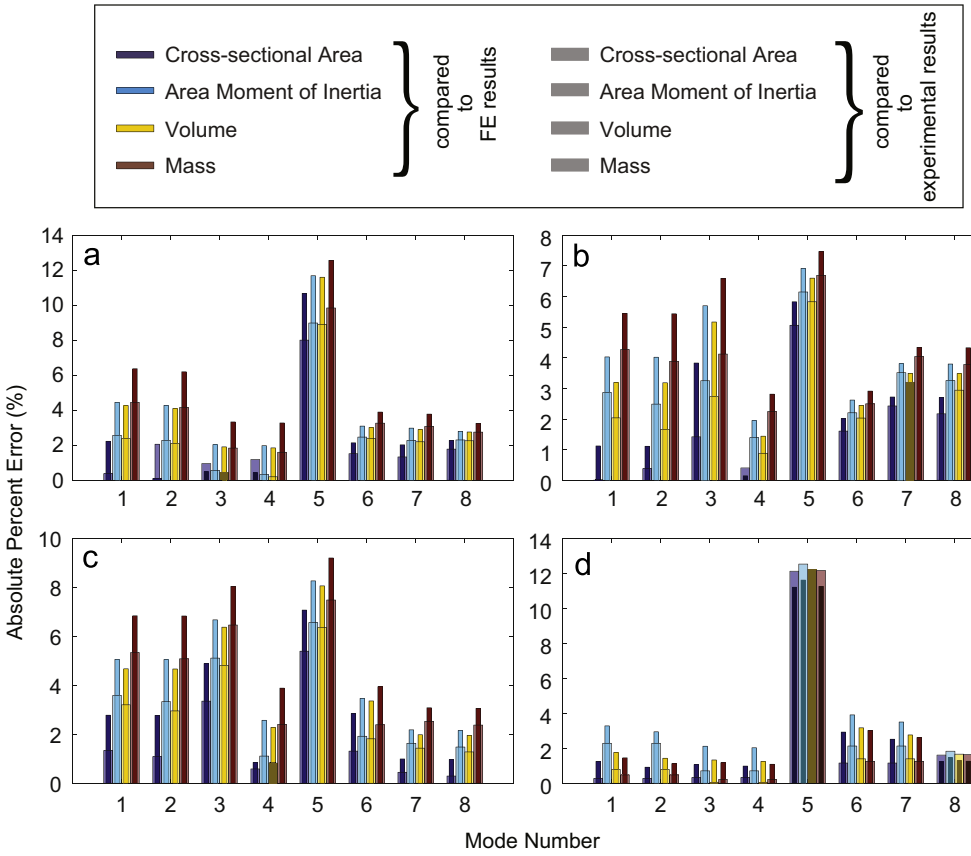

Fig. 8. Absolute percent errors of the approximate methods for (a) endmill 1; (b) endmill 2; (c) endmill 3; (d) endmill 4.

small difference between the 3D-ST and experimental natural frequencies could be the result of differences between the modeled and actual geometry and the non-uniform/inaccurate material properties. Furthermore, it is observed that the largest errors occur in the first torsional mode, which suggests that it is the most sensitive mode to geometric uncertainties. A comparison between natural frequencies from the 3D-ST and FEM results, on the other hand, shows a difference less than 0.8% for all four endmills and modes. This good match between the 3D-ST and FEM results, which use identical geometries and material properties, also supports this hypothesis. It should be noted that the dynamic response is very sensitive to the geometry of the transition region. Therefore, it is critical to accurately capture this geometry.

For a more in-depth assessment of the 3D-ST model, the modal assurance criterion (MAC) was used [20,21]. The modal assurance criterion is a measure of consistency of the modal vectors obtained through two different methods. If the MAC value for a given mode is above 0.8 (i.e., 80%), it is considered that the modes are consistent [21]. Therefore, this method was used to compare the mode shapes (other than rigid body modes) obtained from the 3D-ST method and FEM analysis. To perform the MAC analysis, the position and associated displacement at each FEM node was obtained. Second, the 3D-ST method was used to determine the displacements at the same positions for the given mode shape. The MAC value for each mode was then calculated from

$$MAC = \frac{\left|\{\Phi_A\}^T \{\Phi_{3D-ST}\}^T\right|^2}{\{\Phi_A\}^T \{\Phi_A\} + \{\Phi_{3D-ST}\}^T \{\Phi_{3D-ST}\}}, \quad (29)$$

where Φ_A and Φ_{3D-ST} are the modal matrices obtained through FE analysis (ANSYS®) and the 3D-ST method, respectively.

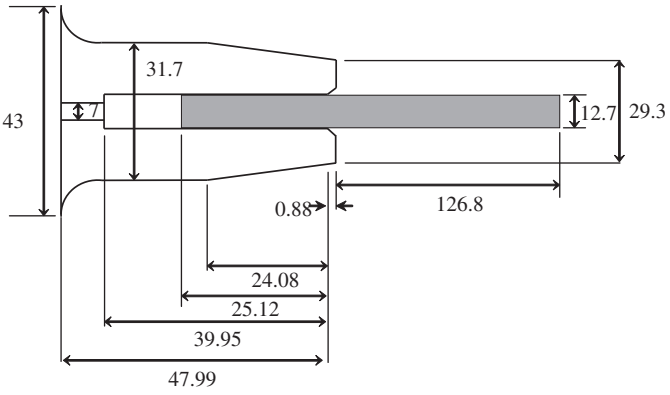

Fig. 9. Holder and blank dimensions for 127.68 mm overhang length (all dimensions are in mm).

Table 6
Carbide endmill/blank and holder material properties.

Component	E (GPa)	$\rho\left(\frac{kg}{m^3}\right)$	ν
Tool	580	14 500	0.24
Holder	200	7800	0.29

The calculated MAC numbers are given in Fig. 7. A MAC number closer to unity indicates good agreement between the mode shapes for the two methods; the first 14 modes of each endmill were analyzed. A good match between the 3D-ST and FEM modes is

observed. A minimum MAC value of 0.855, 0.993, 0.966, and 0.931 and the average MAC values of 0.975, 0.995, 0.992, and 0.989 are obtained for endmills 1, 2, 3, and 4, respectively.

The equivalent diameter simplification for the twisted fluted section of the tool was also evaluated. Fig. 8 provides the percent errors for each of the approximate methods with respect to the results of the FEM results for each mode.

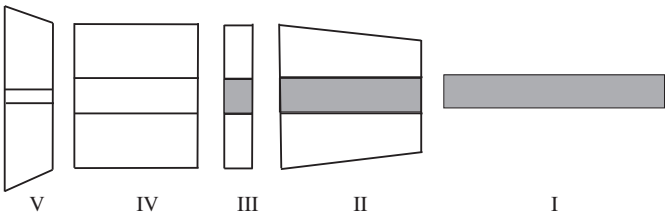

Fig. 10. Blank-holder model components.

Table 7
Component dimensions for 127.68 mm overhang length.

Dimensions (mm)	Component				
	V	*IV*	*III*	*II*	*I*
Outer diameter (d_0), left	43	31.7	31.7	31.7	12.7
Outer diameter (d_0), right	31.7	31.7	31.7	29.3	12.7
Inner diameter (d_i), left	7	12.7	12.7	12.7	0
Inner diameter (d_i), right	7	12.7	12.7	12.7	0
Length, L	8.04	14.83	1.04	24.08	127.68

The general trend of the percent errors was similar for each tool model. Comparing the different approximation methods, the most accurate equivalent diameter was obtained using the cross-sectional area and the least accurate approach was the method based on the endmill mass. Also, considering all four approximation methods for each mode, the largest errors ($>10\%$) was observed for the first torsional mode. Furthermore, the approximation errors depend strongly on the particular geometric parameters of the endmills. Therefore, these approximations should be used carefully. The 3D-ST modeling approach presented in this study avoids such errors while retaining numerical efficiency.

7. Tool point measurements and predictions

Tool point measurements were performed and predictions were completed on a Mikron UCP-600 Vario five-axis machining center. Predictions and measurements of the tool point FRFs are presented here for three different overhang lengths (118.7 mm, 124.78 mm, and 127.59 mm) of endmill 4 (150.8 mm total length) inserted in a steel tapered thermal shrink fit holder. The tool point FRFs were measured by exciting the tool tip with a miniature impact hammer (PCB 0841A17, sensitivity 46.95 N/V) and recording the corresponding vibration with a low mass accelerometer (PCB 352C23, sensitivity 1727 (m/V s^2). Also, measurements were performed with the same shrink fit holder using a carbide blank of approximately the same length as the endmill (152.8 mm). The overhang lengths of the blank were adjusted to match the three overhang lengths of the tool. Fig. 9 shows the dimensions of the holder and blank for an overhang length of 127.68 mm. Table 6

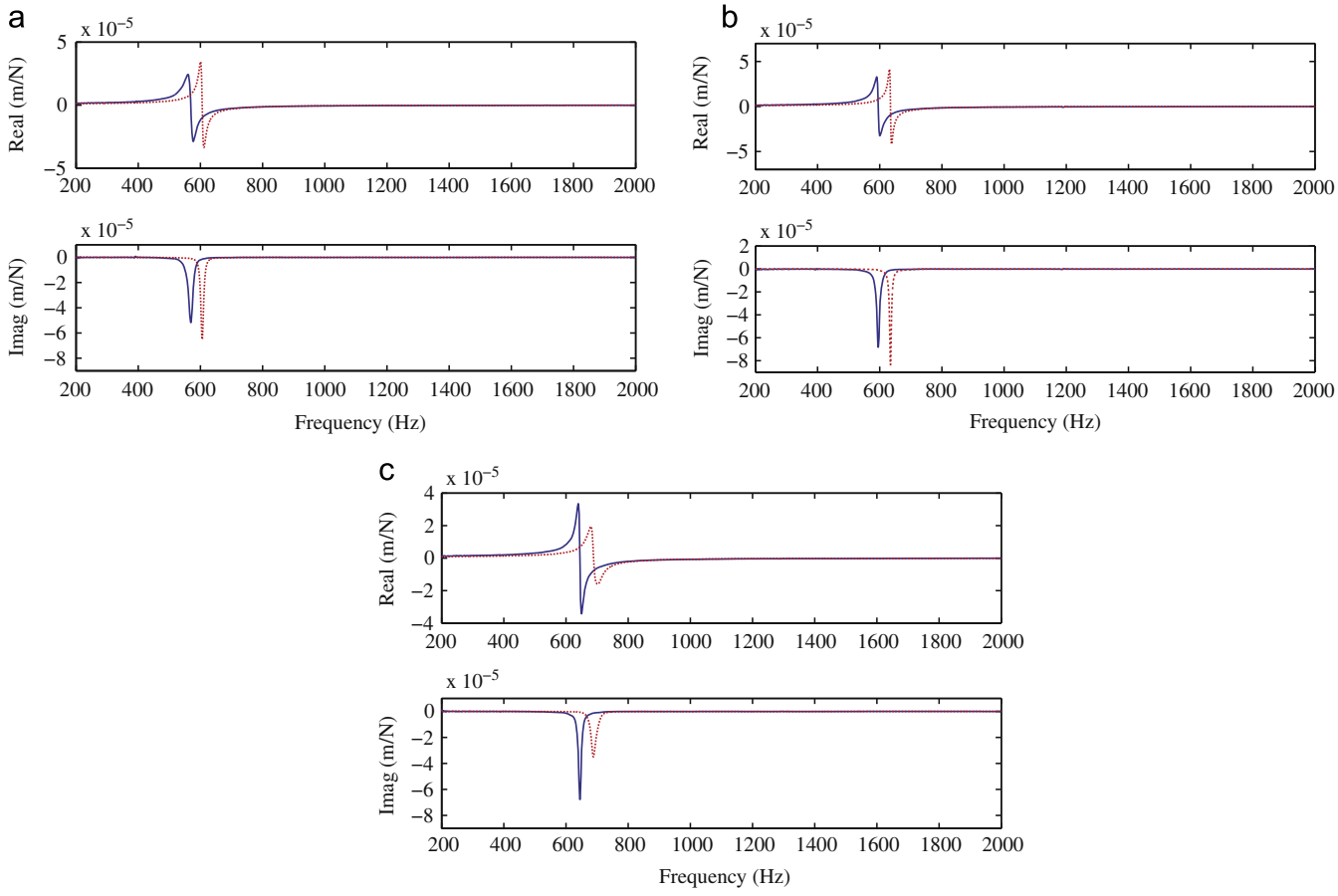

Fig. 11. Measured (solid line) and predicted (dotted line) tool point FRFs for the carbide tool blank with overhang lengths of: (a) 127.68 mm; (b) 124.35 mm; and (c) 118.62 mm (rigid connection).

lists the tool and holder material properties used for modeling both the endmill and blank. The component model for one blank-holder combination is shown in Fig. 10, and the corresponding dimensions are listed in Table 7. Fig. 11 shows the comparison of the measured and the predicted carbide blank tool-point FRF for three different overhang lengths.

It is observed in Fig. 11 that the predicted natural frequencies are higher than those from the experiments. This is attributed to the assumption of a rigid connection between the tool and the holder at coordinate 2 in Fig. 12. Since no connection is rigid in reality, a flexible connection between the tool and the holder was implemented.

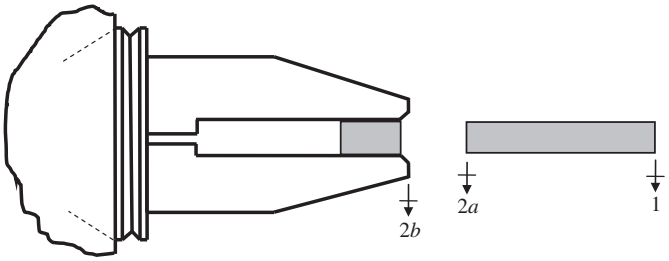

Fig. 12. Component coordinates for flexible coupling in case of blank.

Table 8
Stiffness matrix values.

k_{xf} (N/m)	$k_{\theta f}$ (N/rad)	$k_{\theta m}$ (Nm/rad)
3.05×10^6	3.07×10^6	0

The flexible coupling of the components is carried out in two steps: (1) the spindle–machine is first rigidly coupled to the holder and the portion of the shank inside the holder; (2) the holder–spindle–machine component is then flexibly coupled to the blank outside the holder using translational and rotational spring constants assembled in the stiffness matrix k. The RCSA equation for the flexible coupling tool point FRF in case of the blank is provided in Eq. (30). The stiffness matrix [9] is given by Eq. (31), where k_{xf}, $k_{\theta f}$, k_{xm}, and $k_{\theta m}$ are the displacement-to-force, rotation-to-force, displacement-to-moment, and rotation-to-moment stiffness values, respectively ($k_{\theta f}$ and k_{xm} were assumed equal due to reciprocity).

$$G_{11}(\omega)=R_{11}(\omega)-R_{12a}(\omega)\left[R_{2b2b}(\omega)+R_{2a2a}(\omega)+\frac{1}{k}\right]^{-1}R_{2a1}(\omega), \tag{30}$$

$$k=\begin{bmatrix}k_{xf} & k_{xm}\\ k_{\theta f} & k_{\theta m}\end{bmatrix}. \tag{31}$$

To identify the stiffness matrix, one overhang length of the blank (124.35 mm) was considered and an optimization procedure based on a genetic algorithm [19] was implemented. The variables were the three stiffness values, and the objective function to be minimized is given by Eq. (32), where the difference between the imaginary parts of the measured (m) and predicted (p) tool

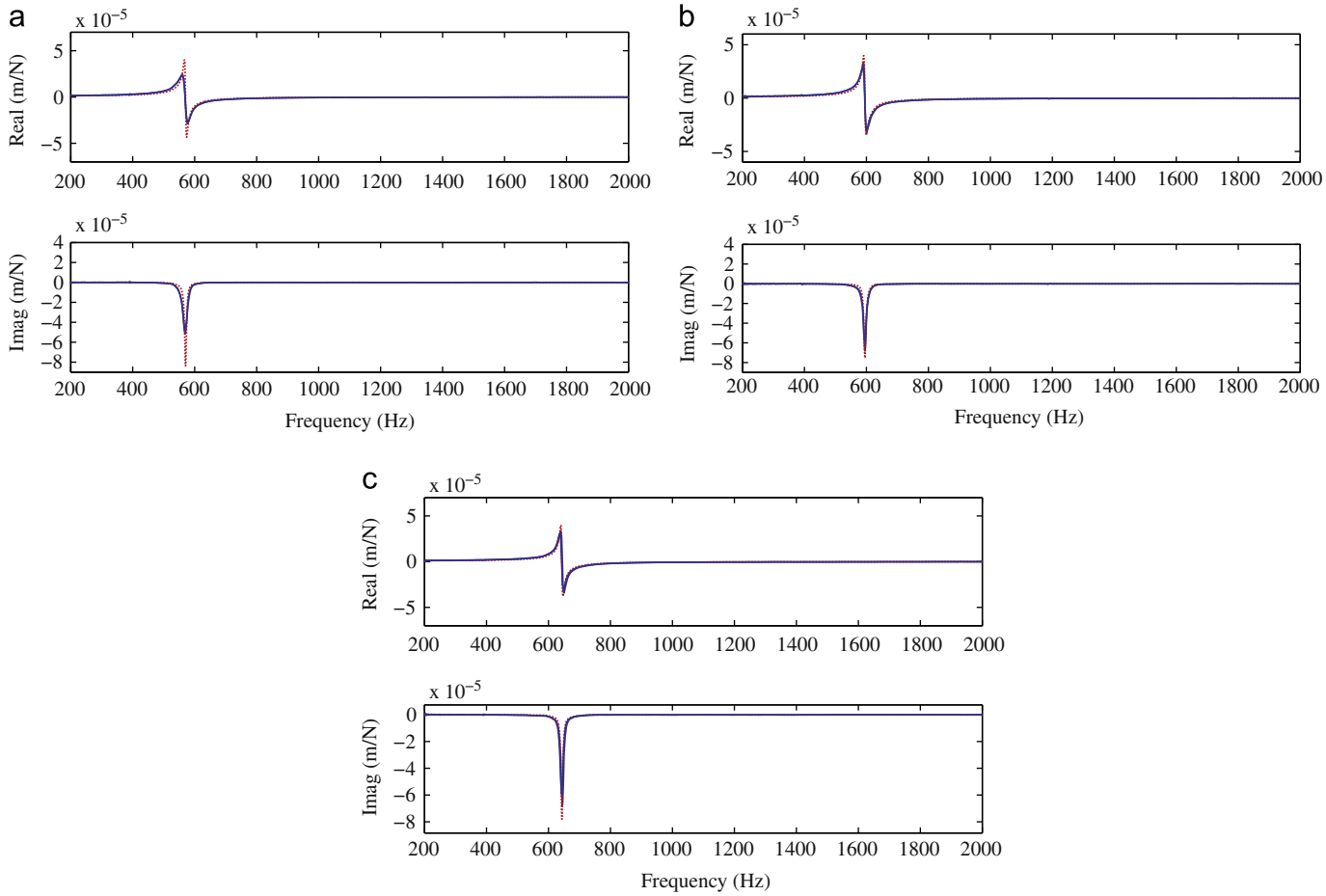

Fig. 13. Measured (solid line) and predicted (dotted line) tool point FRFs for the carbide tool blank with overhang lengths of: (a) 127.68 mm; (b) 124.35 mm; and (c) 118.62 mm (flexible connection).

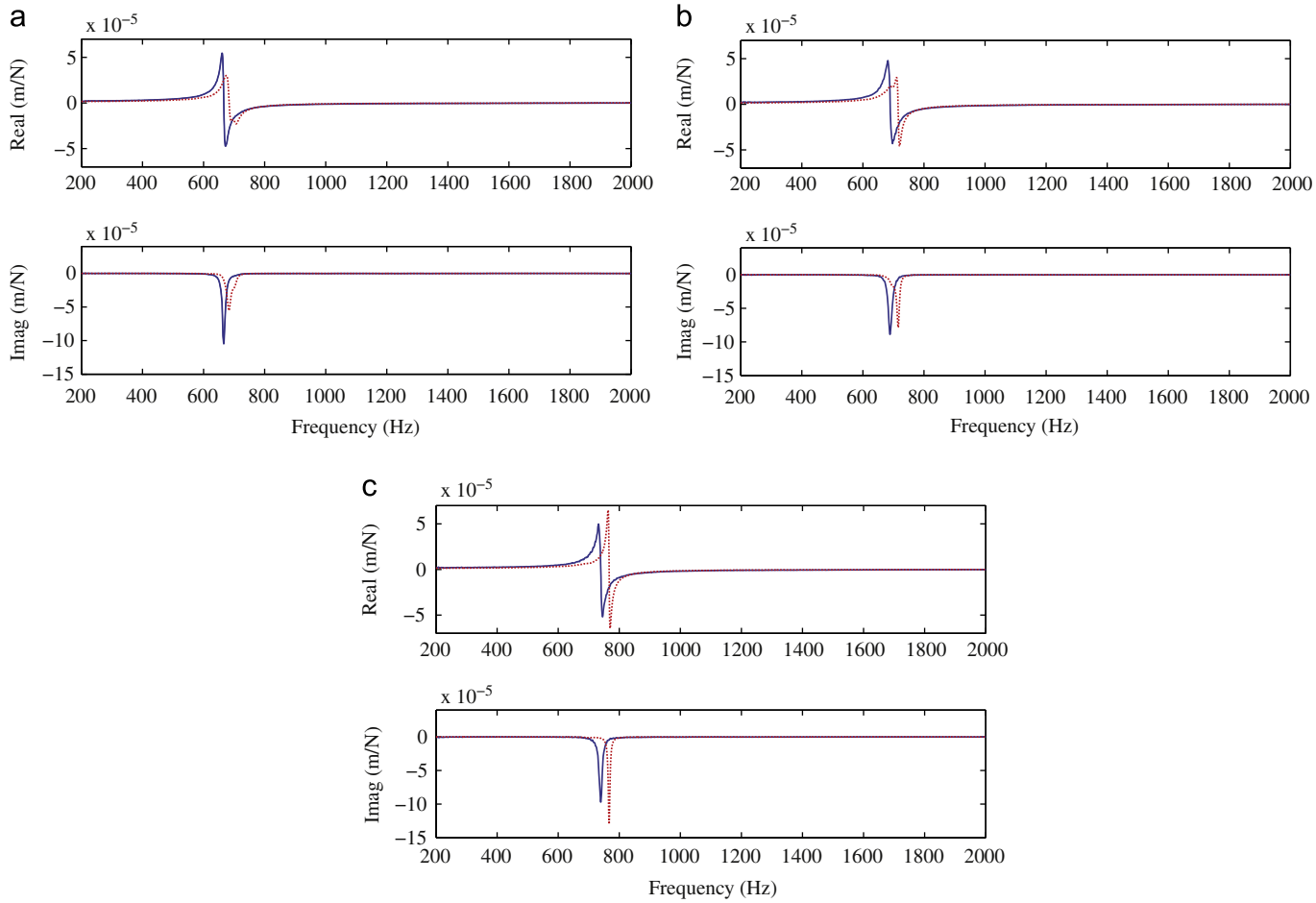

Fig. 14. Measured (solid line) and predicted (dotted line) tool point FRFs for the carbide endmill with overhang lengths of: (a) 127.59 mm; (b) 124.78 mm; and (c) 118.7 mm (flexible connection).

Table 9
Percent error between measurement (M) and prediction (P) for Fig. 13.

Overhang length (mm)	Mode 1		Mode 2		Mode 3		Mode 4	
	M (Hz)	P (Hz)	M (Hz)	P (Hz)	M (Hz)	P (Hz)	M (Hz)	P (Hz)
Fig. 13(a)								
127.68	569.5	570.7	2030	2133.5	3073	2979	3925	3880
% error	−0.2		−5.1		3.1		1.1	
Fig. 13(b)								
124.35	595.1	594.9	2045	2143	3111	3082.3	3800	3890
% error	0.0		−4.8		0.9		−2.4	
Fig. 13(c)								
118.62	644.8	643.2	2060	2155	3230	3264	4087	3909
% error	0.2		−4.6		−1.1		4.4	

Table 10
Percent error between measurement (M) and prediction (P) for Fig. 14.

Overhang length (mm)	Mode 1		Mode 2		Mode 3		Mode 4	
	M (Hz)	P (Hz)	M (Hz)	P (Hz)	M (Hz)	P (Hz)	M (Hz)	P (Hz)
Fig. 14(a)								
127.59	666	682.2	2105	2052	2864	2745.4	3750	3920
% error	−2.5		2.5		4.1		−4.5	
Fig. 14(b)								
124.78	688.4	716	2070	2072	2944	2819	3820	3922
% error	−4.0		−0.1		4.2		−2.7	
Fig. 14(c)								
118.7	739.3	766.8	2090	2094	3087	2987.3	3910	3928
% error	−3.7		−0.2		3.2		−0.5	

point FRFs was squared and summed over all frequencies within the range of interest.

$$\min\left[\sqrt{\sum(Im(H_m)-Im(H_p))^2}\right]. \quad (32)$$

The k matrix values obtained by this approach (see Table 8) were used to predict the tool point FRFs for other overhang lengths of the blank as well as the endmill. The comparison of the measurements and predictions for the three overhang lengths of the carbide blank is shown in Fig. 13. Note that due to the linear axis of the FRF plots in Figs. 13 and 14, the higher modes cannot be observed, however, comparison of four dominant modes was included in the analyses. Table 9 lists the percent errors between the measured and predicted natural frequencies for the four dominant modes within the 5000 Hz measurement bandwidth.

The stiffness values given in Table 8 were used to predict the THSM assembly tool point FRFs for the carbide endmill with different overhang lengths. Fig. 14 shows the measured and predicted results. The percent errors between the predicted natural frequencies and the measured values for the four dominant modes within the 5000 Hz measurement bandwitdh were listed in Table 10 for three overhang lengths.

8. Conclusion

This paper presented new modeling results for the three-dimensional (3D) dynamic behavior of macro-scale milling tools using the spectral-Tchebychev (ST) technique. The actual complex cross-sectional geometry and the pretwisted shape of endmills were taken into account during modeling. The bending and torsional behavior of three endmills with known cross-section was modeled and verified against both finite element models and experiments (impact testing with free–free boundary conditions). Model validation was also performed for a commercial carbide endmill. The difference between the experiments and the spectral-Tchebychev method predictions was seen to be less than 3% for all the four tools for the first six bending modes and first two torsional/axial modes. The natural frequencies from the finite elements model and the 3D-ST method were seen to match with less than 1% difference.

To demonstrate the application of the modeling approach, the 3D-ST model of a commercial carbide endmill was coupled to the Timoshenko beam model of a shrink fit holder and the measured spindle receptances using receptance coupling substructure analysis (RCSA). The tool point measurements and predictions were compared for three different overhang lengths. A flexible connection between the tool and the holder was implemented, where the holder–tool interface stiffness values were determined using a carbide blank and a genetic algorithm-based optimization technique. The stiffness values were used to predict the tool point FRFs of other blanks with different overhang lengths, as well as the endmill with various overhang lengths. The maximum error between the natural frequency of the tool point measurement and prediction was less than 1% for the carbide blank and less than 4% for the endmill.

Acknowledgments

The authors gratefully acknowledge financial support from the National Science Foundation (CMMI-0928393 and CMMI-0928211).

References

[1] J. Tlusty, Manufacturing Processes and Equipment, Prentice Hall, Upper Saddle River, NJ, 2000.
[2] Y. Altintas, Manufacturing Automation: Metal Cutting Mechanics, Machine Tool Vibrations, and CNC Design, Cambridge University Press, Cambridge, UK, 2000.
[3] T. Schmitz, K.S. Smith, Machining Dynamics: Frequency Response to Improved Productivity, Springer, New York, NY, 2009.
[4] T. Schmitz, R. Donaldson, Predicting high-speed machining dynamics by substructure analysis, Annals of the CIRP 49 (1) (2009) 303–308.
[5] T. Schmitz, M. Davies, M. Kennedy, Tool point frequency response prediction for high-speed machining by RCSA, Journal of Manufacturing Science and Engineering 123 (2001) 700–707.
[6] G.S. Duncan, M. Tummond, T. Schmitz, An investigation of the dynamic absorber effect in high-speed machining, International Journal of Machine Tools and Manufacture 45 (2005) 497–507.
[7] T. Schmitz, G.S. Duncan, Three-component receptance coupling substructure analysis for tool point dynamics prediction, Journal of Manufacturing Science and Engineering 127 (4) (2005) 781–790.
[8] T. Schmitz, G.S. Duncan, Receptance coupling for dynamics prediction of assemblies with coincident neutral axes, Journal of Sound and Vibration 289 (4–5) (2006) 1045–1065.
[9] T. Schmitz, K. Powell, D. Won, G.S. Duncan, W.G. Sawyer, J. Ziegert, Shrink fit tool holder connection stiffness/damping modeling for frequency response prediction in milling, International Journal of Machine Tools and Manufacture 47 (9) (2007) 1368–1380.
[10] C.-H. Cheng, G.S. Duncan, T. Schmitz, Rotating tool point frequency response prediction using RCSA, Machining Science and Technology 11 (3) (2007) 433–446.
[11] S. Filiz, C.-H. Cheng, K. Powell, T. Schmitz, O.B. Ozdoganlar, An improved tool-holder model for RCSA tool-point frequency response prediction, Precision Engineering 33 (2009) 26–36.
[12] A. Erturk, H.N. Ozguven, E. Budak, Analytical modeling of spindle-tool dynamics on machine tools using Timoshenko beam model and receptance coupling for the prediction of tool point FRF, International Journal of Machine Tools and Manufacture 46 (2006) 1901–1912.
[13] E. Budak, A. Erturk, H.N. Ozguven, A modeling approach for analysis and improvement of spindle-holder-tool assembly dynamics, Annals of the CIRP 55 (2006) 369–372.
[14] S. Filiz, O.B. Ozdoganlar, A model for bending, torsional, and axial vibrations of micro-and macro-drills including actual drill geometry. Part I: model development and numerical solution, Journal of Manufacturing Science and Engineering 132 (4) (2010) 041017.
[15] S. Filiz, O.B. Ozdoganlar, A model for bending, torsional, and axial vibrations of micro-and macro-drills including actual drill geometry. Part II: model validation and application, Journal of Manufacturing Science and Engineering 132 (4) (2010) 041018.
[16] S. Filiz, O.B. Ozdoganlar, Microendmill dynamics including the actual fluted geometry and set-up errors. Part I: model development and numerical solution, Journal of Manufacturing Science and Engineering 130 (2008) 031119-1.
[17] S. Filiz, O.B. Ozdoganlar, Microendmill dynamics including the actual fluted geometry and set-up errors. Part II: model validation and application, Journal of Manufacturing Science and Engineering 130 (2008) 031120-1.
[18] B. Yagci, S. Filiz, L.L. Romero, O.B. Ozdoganlar, A spectral-Tchebychev technique for solving linear and nonlinear beam equations, Journal of Sound and Vibration 321 (2009) 275–404.
[19] M.R. Movaheddy, J.M. Gerami, Prediction of spindle dynamics in milling by sub-structure coupling, International Journal of Machine Tools & Manufacture 46 (2005) 243–251.
[20] R.J. Allemang, The modal assurance criterion—twenty years of use and abuse, Sound and Vibration (37) (2003) 14–23.
[21] D.J. Ewins, Modal validation: correlation for updating, Sadhana 25 (3) (2000) 221–234.